
A Fixed-point Scheme for the Numerical Construction of Magnetohydrostatic Atmospheres in Three Dimensions

S. A. Gilchrist¹ · D. C. Braun¹ · G. Barnes¹

Abstract Magnetohydrostatic models of the solar atmosphere are often based on idealized analytic solutions because the underlying equations are too difficult to solve in full generality. Numerical approaches, too, are often limited in scope and have tended to focus on the two-dimensional problem. In this article we develop a numerical method for solving the nonlinear magnetohydrostatic equations in three dimensions. Our method is a fixed-point iteration scheme that extends the method of Grad and Rubin (*Proc. 2nd Int. Conf. on Peaceful Uses of Atomic Energy* **31**, 190, 1958) to include a finite gravity force. We apply the method to a test case to demonstrate the method in general and our implementation in code in particular.

1. Introduction

There is a general interest in constructing magnetohydrostatic models of the solar atmosphere. These models describe large-scale, long-lived, magnetic structures like sunspots (*e.g.* Schlüter and Temesváry, 1958), prominences (*e.g.* Kippenhahn and Schlüter, 1957), coronal loops (*e.g.* Zweibel and Hundhausen, 1982),

✉ S.A.Gilchrist
sgilchrist@nwra.com

¹ NorthWest Research Associates (NWRA), 3380 Mitchell Ln., Boulder, CO 80301, USA

the coronal magnetic field on global scales (*e.g.* Bogdan and Low, 1986; Ruan *et al.*, 2008), and low-lying magnetic structures in the upper photosphere and lower chromosphere (*e.g.* Wiegmann *et al.*, 2015). Unfortunately, the equations of the model — the magnetohydrostatic equations — are a set of nonlinear partial differential equations that defy general analytic solution. Only a handful of idealized analytic solutions are known, and existing numerical methods are typically limited to two dimensions. Solution methods for the general three-dimensional equations are lacking, which limits the scope of the modeling. In this article, we present a new numerical scheme for treating the general three-dimensional problem. Our method is an extension of the Grad-Rubin method (Grad and Rubin, 1958) to include a finite gravity force.

The magnetohydrostatic equations describe a magnetized plasma in which magnetic, pressure, and external forces are in mechanical equilibrium. In the solar context, the external force is usually gravity, implying that the condition for mechanical equilibrium is

$$\mathbf{J} \times \mathbf{B} - \nabla p + \rho \mathbf{g} = \mathbf{0} \quad (1)$$

(Priest, 2014), where \mathbf{J} is the electric current density, \mathbf{B} is the magnetic field, p is the gas pressure, ρ is the gas density, and \mathbf{g} is the local acceleration due to gravity. The special case with $\mathbf{g} = \mathbf{0}$ is of interest to modeling fusion plasmas (*e.g.* Spitzer, 1958; Chodura and Schlüter, 1981; Greene and Johnson, 1961), but in this article we consider only the case with a finite gravity force, which is more relevant to modeling the Sun. Since \mathbf{J} is the curl of \mathbf{B} in accordance with Ampère’s law, the force-balance equation is nonlinear through the Lorentz force term. It is this nonlinearity that makes the magnetohydrostatic equations difficult to solve.

Magnetohydrostatic models find various applications in solar physics (*e.g.* Schlüter and Temesváry, 1958; Kippenhahn and Schlüter, 1957; Zweibel and Hundhausen,

1982; Bogdan and Low, 1986; Ruan *et al.*, 2008; Steiner, Pneuman, and Stenflo, 1986; Pneuman and Kopp, 1971). One area where they are becoming increasingly relevant is local helioseismology, where magnetohydrostatic sunspot models are used as the background atmosphere to magnetohydrodynamic wave propagation simulations (*e.g.* Khomenko and Collados, 2006; Khomenko, Collados, and Felipe, 2008; Moradi, Hanasoge, and Cally, 2009; Cameron *et al.*, 2011). The present modeling is based on axisymmetric magnetohydrostatic solutions (see Moradi *et al.*, 2010 for a full list of models) and so is limited to monopolar sunspots. To construct atmospheres for more complex sunspot groups requires more general solution methods.

Data-driven modeling of the coronal magnetic field is another area where three-dimensional magnetohydrostatic models have potential applications. The coronal magnetic field is often “extrapolated” from vector-magnetogram data based on a nonlinear force-free model (*e.g.* Régnier, Amari, and Kersalé, 2002; Thalmann, Wiegelmann, and Raouafi, 2008; Gilchrist, Wheatland, and Leka, 2012; Valori *et al.*, 2012). However, it is known that the magnetogram data represent the magnetic field at a height in the atmosphere where pressure and gravity forces, which the force-free model excludes, are significant (Metcalf *et al.*, 1995; Gary, 2001; Socas-Navarro, 2005). This inconsistency is a potential source of problems for the modeling (DeRosa *et al.*, 2009,2015), and a self-consistent approach based on a magnetohydrostatic model has been suggested as a solution but never applied to actual data (Wiegelmann and Inhester, 2003; DeRosa *et al.*, 2009). To the best of our knowledge, the only magnetohydrostatic extrapolations performed to date have been based on a special class of “linear” magnetohydrostatic solution that assumes a particular functional form for the current density (Low, 1992; Petrie and Neukirch, 2000). These solutions have been used to extrapolate the coronal magnetic field from magnetogram data for several studies (*e.g.* Aulanier *et al.*, 1998, 1999; Petrie, 2000; Wiegelmann *et al.*, 2015)

The nonlinearity of the magnetohydrostatic equations complicates their solution, and no method is known for constructing general analytic solutions. Particular analytic solutions, however, can be derived by simplifying the equations at the expense of generality. One strategy is to reduce the dimensionality of the problem by assuming self-similarity (Schlüter and Temesváry, 1958; Low, 1980), translational symmetry (Zweibel and Hundhausen, 1982), or rotational symmetry (Uchida and Low, 1981). Another approach, which produces three-dimensional solutions, is to impose a special form on either the current density (Low, 1985; Neukirch, 1997; Petrie and Neukirch, 2000) or the magnetic tension (Low, 1984). All these solutions are special cases — the general three-dimensional magnetohydrostatic problem remains unsolved.

A numerical approach can in principle address the shortcomings of the analytic methods. With this goal, a number of numerical methods have been developed, although a majority have only been implemented in two dimensions. These methods include magnetohydrodynamic relaxation methods (*e.g.* Deinzer *et al.*, 1984), fixed-point iteration methods (*e.g.* Pizzo, 1986, 1990), and nonlinear multigrid methods applied to the magnetohydrostatic equations formulated in inverse coordinates (*e.g.* Cally, 1990). This list is not exhaustive: Hennig and Cally (2001) provide a more complete list of references.

Less work has been done on numerical methods for the three-dimensional problem. Hennig and Cally (2001) develop a three-dimensional inverse coordinate nonlinear multigrid method. Their method also solves the free-surface problem for a flux rope bounded by a current sheet. The optimization method that was originally introduced by Wheatland, Sturrock, and Roumeliotis (2000) for solving the nonlinear force-free equations has been extended to treat the magnetohydrostatic equations in Cartesian (Wiegelmann and Inhester, 2003) and spherical coordinates (Wiegelmann *et al.*, 2007).

In this article we develop a fixed-point method for solving the general three-dimensional magnetohydrostatic equations in a Cartesian box. In particular, we extend the method of Grad and Rubin (1958) to model a gravity force. The original Grad-Rubin method solves the magnetohydrostatic equations without gravity by replacing the nonlinear equations by a system of linear equations for each unknown variable, which are solved interactively. The linearization is achieved by constructing nonlinear terms using variables from previous iterations. For example, the Lorentz force is constructed as

$$\nabla \times \mathbf{B}^{[k+1]} \times \mathbf{B}^{[k]}, \quad (2)$$

which is linear in $\mathbf{B}^{[k+1]}$, since $\mathbf{B}^{[k]}$ is known from a previous iteration (the superscript denotes the iteration number). This makes it possible to define a system of linear “update equations” that relate each variable at the current iteration to those known from previous iterations. The update equations are solved successively, and a solution to the complete nonlinear system is obtained when and if the iteration converges to a fixed point. This method has been previously used to solve the magnetohydrostatic equations with $\mathbf{g} = 0$ (Greene and Johnson, 1961; Amari, Boulbe, and Boulmezaoud, 2009; Gilchrist and Wheatland, 2013). It has also been used to solve the nonlinear force-free equations (Sakurai, 1981; Amari, Boulmezaoud, and Mikic, 1999; Wheatland, 2004, 2007), which is the special case of the magnetohydrostatic equations defined by the condition $\mathbf{J} \times \mathbf{B} = 0$. In this article we extend the method to solve the magnetohydrostatic equations with $\mathbf{g} \neq 0$.

Constructing solutions using a fixed-point method has several potential advantages over the methods of Hennig and Cally (2001) and Wiegmann and Inhester (2003). Firstly, unlike methods formulated in inverse coordinates, our method does not fix the topology of the magnetic field *a priori*. Secondly, the method does not overspecify the boundary-value problem like the optimization method.

2. The Magnetohydrostatic Model and Boundary-Value Problem

In this section we describe the details of the magnetohydrostatic model. We present the equations and formulate the magnetohydrostatic boundary-value problem.

The magnetohydrostatic equations in Cartesian coordinates are (Priest, 2014):

$$\mathbf{J} \times \mathbf{B} - \nabla p - \rho g(z) \hat{\mathbf{z}} = 0, \quad (3)$$

$$\nabla \times \mathbf{B} = \mu_0 \mathbf{J}, \quad (4)$$

and

$$\nabla \cdot \mathbf{B} = 0, \quad (5)$$

where \mathbf{B} is the magnetic field, \mathbf{J} is the electric current density, p is the gas pressure, ρ is the gas density, and $g(z)$ is the acceleration due to gravity. For our model we will assume that the force of gravity acts in the negative z direction and is a known function of z .

In addition to Equations (3)–(5), it is also necessary to specify an equation of state and an energy equation to close the system. For the equation of state, we use the ideal gas law,

$$p(\mathbf{r}) = \frac{R}{\tilde{\mu}(\mathbf{r})} \rho(\mathbf{r}) T(\mathbf{r}), \quad (6)$$

where R is the ideal gas constant, and $\tilde{\mu}(\mathbf{r})$ is the mean atomic weight, which may vary with position \mathbf{r} . Since only the ratio $T/\tilde{\mu}$ is important, we introduce the scale height,

$$h(\mathbf{r}) = \frac{RT(\mathbf{r})}{\tilde{\mu}(\mathbf{r})g(z)}, \quad (7)$$

and rewrite the equation of state as

$$p(\mathbf{r}) = g(z)\rho(\mathbf{r})h(\mathbf{r}). \quad (8)$$

The final equation is the steady-state energy equation. A realistic equation, however, is nontrivial to construct. In the interior, energy transport by convection is important, but is difficult to treat self-consistently without modeling flows. Higher in the atmosphere, coronal heating must be treated, which is difficult because the underlying mechanism is uncertain. Although there are some exceptions (Pizzo, MacGregor, and Kunasz, 1993; Fiedler and Cally, 1990), explicit treatment of the energetics is often avoided for these reasons. For example, the method of Wiegelmann *et al.* (2007) models neither an energy equation nor an equation of state, and the method of Pizzo (1986) treats energy transport implicitly by prescribing $h(\mathbf{r})$ in the volume. For our model we adopt the latter approach and prescribe $h(\mathbf{r})$ everywhere in the computational volume.

In summary, the dependent variables of the model are \mathbf{B} , \mathbf{J} , p and ρ . It is assumed that both the scale height $h(\mathbf{r})$ and the acceleration due to gravity $g(z)$ are known everywhere in the volume, and so given either p or ρ , the other is known.

2.1. Domain and Boundary-Value Problem

We solve the model in the finite Cartesian box

$$V = \left\{ (x, y, z) \mid -\frac{L_x}{2} \leq x \leq +\frac{L_x}{2}, -\frac{L_y}{2} \leq y \leq +\frac{L_y}{2}, 0 \leq z \leq +L_z \right\}. \quad (9)$$

The boundary of the domain, ∂V , is formed by the six planar faces of the box. Working in Cartesian coordinates simplifies the numerical implementation, but this geometry is unsuitable for modeling large-scale structures or the global magnetic field because the curvature of the Sun cannot be ignored at these scales. A correct treatment requires an implementation in spherical geometry,

such as the magnetohydrostatic method of Wiegmann *et al.* (2007) or the force-free methods of either Amari *et al.* (2013) or Gilchrist and Wheatland (2014). Nevertheless, the Cartesian implementation can still be useful for structures of active-region size.

To solve the magnetohydrostatic equations, boundary conditions are required on a subset of the dependent variables \mathbf{B} , \mathbf{J} , p , and ρ . Since the pressure and density are related through the ideal gas law and since $h(\mathbf{r})$ is prescribed everywhere, p and ρ are not independent — fixing both independently at the boundary is an overspecification. Of the two, we prescribe boundary conditions on p .

All that remains is to specify the exact form of the boundary conditions on \mathbf{B} , \mathbf{J} and p . We follow the approach of Grad and Rubin (1958), who consider different formulations of the boundary-value problem for the special case with $\mathbf{g} = 0$. The Grad-Rubin boundary conditions are the normal component of \mathbf{B} ,

$$\mathbf{B} \cdot \hat{\mathbf{n}}|_{\partial V} = B_n, \quad (10)$$

the normal component of \mathbf{J} ,

$$\mathbf{J} \cdot \hat{\mathbf{n}}|_{\pm\partial V} = J_n, \quad (11)$$

and the pressure distribution,

$$p|_{\pm\partial V} = p_0. \quad (12)$$

Here $\pm\partial V$ is either $+\partial V$ or $-\partial V$, which are the subsets of ∂V where $B_n > 0$ and where $B_n < 0$ respectively. This means that the boundary conditions on the pressure and current density are prescribed either at points in the boundary where $B_n > 0$ or at points in the boundary where $B_n < 0$, but not both. The reason for this is that pressure and the field-aligned component of the current density obey hyperbolic transport equations along field lines (see Grad and Ru-

bin, 1958), and thus boundary conditions on J_n and p must only be prescribed at one end of each field line to avoid overspecification of the boundary-value problem.

In formulating the boundary-value problem, we also make the assumption that all field lines are connected to the boundary. This is again related to the hyperbolic character of the underlying equations — information in the boundary is transported into the volume along magnetic field lines, meaning points not connected to the boundary are undetermined. Formulations that account for closed field lines are possible and are discussed by Grad and Rubin (1958). Since closed field lines are not considered, imposing boundary conditions at points where $B_n = 0$ is also an overspecification, as field lines threading these points cross the boundary elsewhere, and therefore prescribing boundary conditions where $B_n = 0$ violates the requirement that there be only one set of boundary conditions *per* field line.

Here we have presented a basic formulation of the boundary-value problem, however more complicated “self-consistency” methods that involve the solution of a sequence of boundary-value problems have been developed for the force-free equations (Wheatland and Régnier, 2009). We note that a similar approach could be developed for the magnetohydrostatic problem.

2.2. Pressure and Density Decomposition

Rather than working with p and ρ directly, it is advantageous to reformulate the magnetohydrostatic equations in terms of the deviation from a gravitationally stratified background atmosphere. The pressure and density deviation due to the magnetic field can be orders of magnitude smaller than the pressure and density of the background and therefore are difficult to resolve numerically. In fact, the difference in magnitudes can lead to numerical instability, as discussed in Appendix A. Splitting p and ρ into background and magnetohydrostatic com-

ponents and computing each separately mitigates this problem.

The magnetohydrostatic equations are linear in p and ρ , so we may write

$$p(\mathbf{r}) = p_{\text{hs}}(z) + p_{\text{mhs}}(\mathbf{r}), \quad (13)$$

and

$$\rho(\mathbf{r}) = \rho_{\text{hs}}(z) + \rho_{\text{mhs}}(\mathbf{r}), \quad (14)$$

where $p_{\text{hs}}(z)$ and $\rho_{\text{hs}}(z)$ are due to a background atmosphere and p_{mhs} and ρ_{mhs} are the variations due to the presence of the magnetic field. Note that the magnetohydrostatic components can be negative.

The background pressure and density satisfy the hydrostatic force-balance equation

$$\frac{dp_{\text{hs}}}{dz} = -g(z)\rho_{\text{hs}}(z), \quad (15)$$

and the equation of state

$$p_{\text{hs}}(z) = g(z)\rho_{\text{hs}}(z)h_{\text{hs}}(z) \quad (16)$$

where $h_{\text{hs}}(z)$ is the scale height for the background atmosphere. To uniquely determine p_{hs} and ρ_{hs} , it is necessary to prescribe the scale height $h_{\text{hs}}(z)$ in the volume and the pressure at either the top or bottom boundary, *i.e.*

$$p_{\text{hs}}|_{z=0/L_z} = p_{0\text{hs}}. \quad (17)$$

From a purely mathematical standpoint, $h_{\text{hs}}(z)$ and $p_{0\text{hs}}$ may be chosen with some freedom. However, for numerical reasons, we choose to construct p_{hs} and ρ_{hs} as the pressure and density of the “quiet Sun” and p_{mhs} and ρ_{mhs} as deviations from this background. In this context “quiet Sun” refers to regions where the magnetic field is negligible. This interpretation of p_{hs} and ρ_{hs} requires that h_{hs}

be the asymptotic form of $h(\mathbf{r})$ in regions where the magnetic field is small. With this choice, p_{mhs} and ρ_{mhs} are generally small in weak-field regions, which turns out to be important numerically (see Appendix A).

With the pressure and density split, the magnetohydrostatic force-balance equation becomes

$$\mathbf{J} \times \mathbf{B} - \nabla p_{\text{mhs}} - \rho_{\text{mhs}} g(z) \hat{\mathbf{z}} = 0, \quad (18)$$

and the ideal gas law becomes

$$p_{\text{mhs}} = g(z) h(\mathbf{r}) \rho_{\text{mhs}}(\mathbf{r}) + g(z) [h_{\text{hs}}(z) - h(\mathbf{r})] \rho_{\text{hs}}. \quad (19)$$

The boundary conditions for p_{mhs} are then

$$p_{\text{mhs}}|_{\pm\partial V} = p_0 - p_{\text{hs}}|_{\pm\partial V}. \quad (20)$$

We use the split form of the magnetohydrostatic equations to formulate our fixed-point iteration.

3. Iteration Scheme

In this section we describe the fixed-point iteration scheme for solving the boundary value problem presented in Section 2.1. The numerical implementation of the method is presented later in Section 4.

To solve the model presented in Section 2, we employ an iterative scheme that extends the method of Grad and Rubin (1958) to include a gravity force. The method replaces the system of nonlinear equations with a set of linear equations that are easier to solve than the original nonlinear ones. The linear equations are solved iteratively and the solution to the nonlinear system is obtained when (and if) the iteration reaches a fixed point.

In the following we describe the steps in a single iteration of the method. We denote a variable after k iterations by a superscript in square brackets, *e.g.* $\mathbf{B}^{[k]}$ denotes the magnetic field after k iterations. In addition, we describe the magnetic field used to initialize the method.

3.1. Initial Magnetic Field

In principle the iteration can be initiated with any magnetic field that satisfies the boundary conditions given by Equation (10), but in practice the simplest field to use is a current-free (potential) magnetic field $\mathbf{B}^{[0]} = \mathbf{B}_0$. This choice may be suboptimal, as other choices, like a nonlinear force-free field, may lie closer to the fixed-point and therefore reduce the number of iterations required to reach a solution. The advantage of using a potential field is that it is straightforward and fast to compute.

The potential field is found by solving the magnetostatic equations (Priest, 2014)

$$\nabla \cdot \mathbf{B}_0 = 0 \tag{21}$$

and

$$\nabla \times \mathbf{B}_0 = 0, \tag{22}$$

subject to the boundary conditions

$$\mathbf{B}_0 \cdot \hat{\mathbf{n}}|_{\partial V} = B_n. \tag{23}$$

Since the normal component of the magnetic field is prescribed on all six boundaries, it is necessary that the net flux over all the boundaries be zero in order for \mathbf{B}_0 to be solenoidal in the volume.

3.2. Iteration Steps

A single iteration of the scheme involves five steps. At each step the new value of a variable is computed by solving either an algebraic or differential equation. It is assumed that at the start of each iteration the magnetic field from the previous iteration is known. The potential field described in Section 3.1 is used for the first iteration. In addition, it is assumed that ρ_{hs} and p_{hs} have been computed beforehand.

Here we enumerate the steps for a single iteration with iteration number k . The updated variables have iteration number $k + 1$. The steps are as follows.

- i) Calculate $p_{\text{mhs}}^{[k+1]}$, the pressure in the volume, by solving

$$\nabla p_{\text{mhs}}^{[k+1]} \cdot \mathbf{B}^{[k]} = \left(\frac{B_z^{[k]}}{h(\mathbf{r})} \right) p_{\text{mhs}}^{[k+1]} + \left(\frac{p_{\text{hs}}}{h(\mathbf{r})} - \rho_{\text{hs}}(z)g(z) \right) B_z^{[k]}, \quad (24)$$

subject to the boundary conditions for p_{mhs} described in Section 2.1. Since ρ_{hs} , p_{hs} , $h(\mathbf{r})$, $g(z)$, and $B_z^{[k]}$ are known, Equation (24) is linear.

- ii) Calculate $\rho_{\text{mhs}}^{[k+1]}$, the gas density in the volume, by direct application of the ideal gas law

$$\rho_{\text{mhs}}^{[k+1]} = \frac{p_{\text{mhs}}^{[k+1]}}{g(z)h(\mathbf{r})} + \frac{p_{\text{hs}}}{g(z)} \left(\frac{1}{h(\mathbf{r})} - \frac{1}{h_{\text{hs}}(z)} \right). \quad (25)$$

- iii) Calculate $\mathbf{J}_{\perp}^{[k+1]}$, the component of current density that is perpendicular to the magnetic field, in the volume. This is computed as

$$\mathbf{J}_{\perp}^{[k+1]} = \frac{-\nabla p_{\text{mhs}}^{[k+1]} \times \mathbf{B}^{[k]} + \rho_{\text{mhs}}^{[k+1]} \mathbf{g} \times \mathbf{B}^{[k]}}{\|\mathbf{B}^{[k]}\|^2}. \quad (26)$$

iv) Calculate $\mathbf{J}_{\parallel}^{[k+1]}$, the component of the current density that is parallel to the magnetic field, in the volume. This component can be expressed as

$$\mathbf{J}_{\parallel}^{[k+1]} = \sigma^{[k+1]} \mathbf{B}^{[k]}, \quad (27)$$

where $\sigma(\mathbf{r})^{[k+1]}$ is a scalar function that varies with position and satisfies the hyperbolic equation

$$\nabla \sigma^{[k+1]} \cdot \mathbf{B}^{[k]} = -\nabla \cdot \mathbf{J}_{\perp}^{[k+1]}. \quad (28)$$

The component $\mathbf{J}_{\parallel}^{[k+1]}$ is found by solving Equation (28) subject to boundary conditions derived from those on J_n and B_n , *i.e.*

$$\sigma^{[k+1]} \Big|_{\pm\partial V} = \frac{\mathbf{J}_{\perp}^{[k+1]} \cdot \hat{\mathbf{n}} - J_n}{B_n} \Big|_{\pm\partial V}. \quad (29)$$

v) Calculate $\mathbf{B}^{[k+1]}$, the new magnetic field in the volume, by solving Ampère's law,

$$\nabla \times \mathbf{B}^{[k+1]} = \mu_0 \mathbf{J}^{[k+1]}, \quad (30)$$

subject to the solenoidal condition

$$\nabla \cdot \mathbf{B}^{[k+1]} = 0, \quad (31)$$

and the boundary conditions on the normal component described in Section 2.1. The current density in Equation (30) is constructed from the components calculated in steps iii) and iv), *i.e.*

$$\mathbf{J}^{[k+1]} = \mathbf{J}_{\perp}^{[k+1]} + \sigma^{[k+1]} \mathbf{B}^{[k+1]} / \mu_0. \quad (32)$$

4. Numerical Implementation

This section describes the implementation of the scheme presented in Section 3 in code.

The code is written in a combination of the Fortran 2008 (Metcalf, Reid, and Cohen, 2011) and C programming languages. It is parallelized for shared-memory parallel computers using OpenMP (Chandra *et al.*, 2001). The code supports calculations in either single, double, extended, or quadruple precision, although use of the latter two slows the calculation.

The numerical mesh is constructed so that the spacing is uniform in any particular dimension but may differ between dimensions. In units of grid points, the domain has the total volume $N_x \times N_y \times N_z$. Each mesh point is

$$(x_i, y_j, z_k) = (i\Delta_x, j\Delta_y, k\Delta_z), \quad (33)$$

where $0 \leq i < N_x$, $0 \leq j < N_y$, and $0 \leq k < N_z$. The grid spacing in each dimension is

$$\Delta_l = \frac{L_l}{N_l - 1}, \quad (34)$$

where $l = x, y$, or z .

4.1. Solution of Elliptic Equations

Calculation of both the potential field and the non-potential field requires the solution of a set of elliptic partial differential equations. By introducing the appropriate scalar and vector potentials, both problems can be reduced to the problem of solving Poisson's equation.

For the potential field calculation we introduce the scalar potential, ϕ_m , defined by

$$\mathbf{B}_0 = \nabla\phi_m. \quad (35)$$

This reduces the problem of solving the potential-field boundary-value problem from Section 3.1 to solving Laplace's equation

$$\nabla^2\phi_m = 0, \quad (36)$$

subject to the Neumann boundary conditions,

$$\nabla\phi_m \cdot \hat{\mathbf{n}}|_{\partial V} = B_n. \quad (37)$$

For the magnetic field calculation in step v), only the non-potential component of the magnetic field needs to be updated. For this reason, we express $\mathbf{B}^{[k+1]}$ as

$$\mathbf{B}^{[k+1]} = \mathbf{B}_0 + \nabla \times \mathbf{A}_c^{[k+1]}, \quad (38)$$

where \mathbf{B}_0 is the potential field defined in Section 3.1, and $\mathbf{A}_c^{[k+1]}$ is a magnetic vector potential. In the Coulomb gauge ($\nabla \cdot \mathbf{A}_c^{[k+1]} = 0$), $\mathbf{A}_c^{[k+1]}$ is a solution of Poisson's equation,

$$\nabla^2 \mathbf{A}^{[k+1]} = -\mu_0 \mathbf{J}^{[k+1]}. \quad (39)$$

Since \mathbf{B}_0 is constructed to satisfy the boundary conditions defined by Equation (10), it follows that the normal component of the non-potential component must vanish on the boundary. The boundary conditions on $\mathbf{A}_c^{[k+1]}$ that achieve this are:

$$\mathbf{A}_c^{[k+1]} \times \hat{\mathbf{n}}|_{\partial V} = 0, \quad (40)$$

and

$$\hat{\mathbf{n}} \cdot \nabla(\mathbf{A}_c^{[k+1]} \cdot \hat{\mathbf{n}})|_{\partial V} = 0. \quad (41)$$

Similar to Pizzo (1986), we employ under relaxation during the magnetic-field-update step in order to improve the numerical stability, *i.e.* rather than update $\mathbf{B}^{[k+1]}$ directly, we set

$$\mathbf{B}^{[k+1]} = (1 - \omega)\mathbf{B}^{[k]} + \omega(\mathbf{B}_0 + \nabla \times \mathbf{A}_c^{[k+1]}), \quad (42)$$

where ω is a constant in the range $(0, 1]$. We find in practice that this improves stability of the iteration scheme without altering the fixed point.

Many numerical methods exist for solving the Laplace and Poisson equations (Press *et al.*, 2007). We use a second-order finite difference multigrid scheme (Briggs, Henson, and McCormick, 2000). The method is fast and scales well. For a mesh with uniform spacing in all dimensions, the time to compute the solution has $\sim N^3$ scaling, where $N_x = N_y = N_z = N$.

4.2. Solution of Hyperbolic Equations

We employ a characteristic (field line tracing) method to solve the hyperbolic equations. We only present the numerical solution of Equation (24), as the method for Equation (28) is similar. The partial differential equation, Equation (24), can be recast as a system of ordinary differential equations along each field line, *i.e.* the equation for $p_{\text{mhs}}^{[k+1]}$ can be expressed as

$$\frac{dp_{\text{mhs}}}{ds} + F(s)p_{\text{mhs}} = G(s), \quad (43)$$

where

$$F(s) = \frac{B_z(s)}{\|\mathbf{B}(s)\|h(s)} \quad (44)$$

and

$$G(s) = \left(\frac{p_{\text{hs}}(s)}{h(s)} - \rho_{\text{hs}}(s)g(s) \right) \frac{B_z(s)^{[k]}}{\|\mathbf{B}(s)^{[k]}\|}. \quad (45)$$

Here d/ds is the derivative along the length of a magnetic field line whose path is a solution of the field line equation

$$\frac{d\mathbf{x}(s)}{ds} = \frac{\mathbf{B}^{[k]}}{\|\mathbf{B}^{[k]}\|}, \quad (46)$$

where $\mathbf{x}(s) = (x(s), y(s), z(s))$ is the Cartesian position along the field line.

The pressure is updated at each step by solving Equations (43) and (46) for each point in the volume. For each mesh point (x_i, y_i, z_i) in the volume, we solve Equation (46) to determine the path of the field line that threads (x_i, y_i, z_i) while simultaneously integrating Equation (43) along this path. The calculation is halted when the field line crosses the boundary of the domain. We perform the calculation in both directions along the field lines and only impose boundary conditions at the endpoint on the boundary with the correct polarity for the boundary conditions.

We perform the integration using a fourth-order Runge-Kutta integrator with a fixed step size (Press *et al.*, 2007). Since the path of the field line is not restricted to the numerical grid, trilinear interpolation is used to compute \mathbf{B} , and h during the integration (Press *et al.*, 2007). We use an “event-location” method that combines interpolation and root finding to determine the location where the field line crosses the boundary (Hairer, Nørsett, and Wanner, 1993).

Solving the hyperbolic system using Runge-Kutta methods is nontrivial because it is not a standard initial-value problem: $p_{\text{mhs}}^{[k+1]}$ is unknown at the initial point $s = 0$. Instead it is a boundary-value problem with boundary conditions on $p_{\text{mhs}}^{[k+1]}$ and $\mathbf{x}(s)$ known at different ends of each field line. At the start of the field line ($s = 0$), the value of $\mathbf{x}(s)$ is known, *i.e.* $\mathbf{x}(0) = (x_i, y_j, z_k)$, but the value of $p_{\text{mhs}}^{[k+1]}(0)$ is not, in fact, this is the value we wish to compute. At the point where the field line crosses the boundary ($s = s_0$), $p_{\text{mhs}}^{[k+1]}(s_0)$ is known from the boundary conditions on p_{mhs} , but the crossing point $\mathbf{x}(s_0)$ is a priori unknown.

In this form the boundary-value problem cannot be solved using standard numerical methods for ordinary-differential equations (*e.g.* Runge-Kutta methods). To solve this problem, we introduce two auxiliary initial-value problems whose solutions, when combined, give the solution to the boundary-value problem. The auxiliary problems are of the standard form and can be treated with standard integration methods. This method is explained in Appendix B.

4.3. Construction of the Background Atmosphere

The background atmosphere is constructed by solving Equation (15) using numerical quadrature. In order that h_{hs} approaches $h(\mathbf{r})$ in weak-field regions (see discussion in Section 2.2) we take

$$h_{\text{hs}}(z) = h\left(-\frac{L_x}{2}, -\frac{L_y}{2}, z\right), \quad (47)$$

where the point $(x, y) = (-L_x/2, -L_y/2)$ is at the edge of the computational volume defined by Equation (9). For the boundary conditions for Equation (15), we take

$$p_{\text{hs}}|_{z=0} = p_0\left(-\frac{L_x}{2}, -\frac{L_y}{2}\right). \quad (48)$$

With this choice it is necessary that regions of strong magnetic field be isolated from the boundaries. We use this corner point to define the background field for the calculations presented here, but it may not be appropriate in all cases and other choices are possible.

We have chosen to compute the background atmosphere using numerical quadrature as this method is applicable when $h_{\text{hs}}(z)$ is given in table form, which is the case for many popular model atmospheres (*e.g.* Vernazza, Avrett, and Loeser, 1981). The code is not restricted to using tabulated background atmospheres and can use analytic background atmospheres too.

4.4. Other Equations

The other steps involve the straightforward evaluation of algebraic equations. The exception is step iii), which requires the evaluation of numerical derivatives. We use a fourth-order finite-difference method to evaluate derivatives (Press *et al.*, 2007). In addition, when computing \mathbf{J}_\perp we use a “safety factor” η in the denominator

$$\mathbf{J}_\perp^{[k+1]} = \frac{-\nabla p_{\text{mhs}}^{[k+1]} \times \mathbf{B}^{[k]} + \rho_{\text{mhs}}^{[k+1]} \mathbf{g} \times \mathbf{B}^{[k]}}{\|\mathbf{B}^{[k]}\|^2 + \eta}. \quad (49)$$

This is needed in weak-field regions, where the truncation error in the numerical derivative can have a similar effect to that discussed in Appendix A.

5. Application of the Method to an Analytic Test Case

We apply our code to a problem with a known analytic solution in order to test the fixed-point method in general and our implementation in code in particular. The goal is to show firstly that the scheme converges to a fixed point, and secondly that the numerical solution obtained thereby is consistent with the known solution within the margins of numerical error. In this way we establish that both the method and our code work. We perform calculations at four different resolutions to demonstrate the scaling of the numerical truncation error. We also determine how the total execution time of the code scales with grid size.

The calculation is performed in non-dimensional units, but here we use dimensional quantities expressed in terms of unspecified characteristic values. For example, the domain size is given as $L_x = 30L_c$, where L_c is unspecified.

5.1. Test Case and Calculation Parameters

To test the code we use the analytic magnetohydrostatic sunspot model of Low (1980), which belongs to the class of self-similar solutions found by Schlüter and

Temesváry (1958). In cylindrical polar coordinates, the magnetic field for this solution is

$$\mathbf{B} = 2B_0 \exp\left(-\frac{R^2}{a^2 + z^2}\right) \left[\frac{Rz}{(a^2 + z^2)^2}, 0, \frac{1}{a^2 + z^2} \right] \quad (50)$$

(Low, 1980), where $R^2 = x^2 + y^2$, a is a free parameter that sets the width of the spot, and B_0 is a free parameter that determines the maximum field strength. The solution is axisymmetric and untwisted ($\sigma \equiv 0$).

For the tests, we use a solution with $a = 5L_c$, and $B_0 = a^2 B_c$, where L_c and B_c are an unspecified characteristic length scale and magnetic field strength, respectively. The dimensions of the domain are $L_x = L_y = 30L_c$, and $L_z = 5L_c$. We perform four calculations at different resolutions with 20 iterations of the method applied starting from a potential field in each case. The number of grid points in each direction are equal, *i.e.* $N_x = N_y = N_z = N$, but N takes the values 64, 96, 128, and 256 in the four cases.

5.2. Convergence of the Fixed-point Scheme

We first demonstrate that the iteration has converged to a fixed point by measuring the change in the magnetic field between iterations using the metric

$$\Delta^{[k]} B_{\max} = \max(|\mathbf{B}^{[k+1]} - \mathbf{B}^{[k]}|), \quad (51)$$

where $||$ is the componentwise absolute value not the vector norm, and $\max()$ is the maximum value over the domain and three components. The value of $\Delta^{[k]} B_{\max}$ is an upper bound on the pointwise change and is therefore small only when the change at every point is small. We regard an iteration as converged when $\Delta^{[k]} B_{\max}$ becomes small. This is a strict measure of convergence, as $\Delta^{[k]} B_{\max}$ will not decrease unless all three components of $\mathbf{B}^{[k]}$ converge to a solution at every point in the volume.

Figure 1 shows $\Delta^{[k]}B_{\max}$ *versus* iteration number k for the four test cases. In each case, $\Delta^{[k]}B_{\max}$ decreases monotonically by about six orders of magnitude over 20 iterations. Given the small value of $\Delta^{[k]}B_{\max}$, we regard the iteration as converged in all four cases.

5.3. Measurements of the Numerical Truncation Error

We next measure the numerical truncation error by comparing the numerical solution at iteration 20 to the known analytic solution. To measure the difference between the analytic and numerical solutions, we use the two metrics

$$u_{\max} = \max(|\mathbf{B} - \mathbf{b}|) \quad (52)$$

and

$$u_{\text{avg}} = \langle |\mathbf{B} - \mathbf{b}| \rangle, \quad (53)$$

where \mathbf{b} is the analytic solution, and the operator $\langle \cdot \rangle$ is the average of $|\cdot|$ over the domain and three components. As in Section 5.2, $|\cdot|$ is the componentwise absolute value. These metrics measure the maximum and average truncation errors respectively.

It should be noted that u_{\max} is a particularly strict measure of the numerical error, since a discrepancy at a single point can significantly affect its value. We have chosen to use this metric as it is useful in detecting errors in the implementation of the boundary conditions. A systematic, resolution independent error at each of the N^2 points in a boundary layer introduces an error with scaling $\sim 1/N$ when averaged over the whole N^3 points in the domain. Hence, the scaling of u_{avg} cannot necessarily distinguish between a method that has $\sim 1/N$ truncation error in the volume, and a method that systematically fails at the boundary, due to, for example, coding errors. This is why we measure both the scaling for u_{\max} and u_{avg} — the metric u_{\max} will not decrease with N if systematic errors at the boundaries exist.

Figure 2 shows the truncation error *versus* N , the number of mesh points along each dimension. The top panel shows u_{\max} *versus* N (circles). The solid line is a power-law fit to the data with power-law index -1.35 . The bottom panel shows u_{avg} *versus* N (circles). The solid line shows a power-law fit with power-law index -1.55 . Based on a visual inspection, there is good agreement between the fitted power-laws and the data in both panels, although the value of u_{\max} at $N = 256$ is larger than the prediction of the fit.

In addition to comparing the analytic and numerical solutions via metrics, it is important to perform a visual comparison between the field lines, as this gives some indication of how the numerical error is distributed spatially. Figure 3 shows a comparison between the field lines of the exact solution (blue lines) and the numerical solution at different resolutions and iteration numbers (red lines). Panels (a) and (c) show the field lines of the exact solution (blue lines) *versus* the field lines of the initial potential field (red lines) for the $N = 64$ and $N = 256$ calculations, respectively. Panels (b) and (d) show the field lines of the exact solution *versus* the field lines of the numerical solutions after 20 iterations of the method (red field lines) for the $N = 64$ and $N = 256$ calculations respectively. In all panels, the field lines are confined to the $x - z$ plane through the origin and only the subdomain with $x \in [0, L_x/2]$ is shown. Since the solution is axisymmetric, the two-dimensional slice gives a good indication of the solution in general. The tracing is initiated from starting points spaced equally along the x axis at $z = 0$. The background image of each panel depicts $\|\mathbf{B}^{[k]}\|$. We note that in the corners where the numerical and exact solutions are most discrepant, the magnetic field strength is smaller than that near the center by several orders of magnitude.

It is also important to check the numerical error in the thermodynamic quantities. Figure 4 shows maps of the quantity

$$\Delta p = \frac{|p_a - p|}{|p_a + p|}, \quad (54)$$

where p_a is the analytic solution, and $||$ is the absolute value. The top panel shows Δp for the $N = 64$ case, and the bottom panel shows Δp for the $N = 256$ case. In both panels we only show a slice through the $x - z$ plane as in Figure 3.

5.4. Measurements of the Total Calculation Time

Finally, we compute the total time required to perform 20 iterations of the method on an eight-core processor. Figure 5 shows the total run time in seconds *versus* N . A power-law fit to the data has a power-law index of 4.2 meaning the run time has approximate $\sim N^4$ scaling.

6. Discussion and Conclusion

We present a new fixed-point iteration method for solving the magnetohydrostatic equations in a three-dimensional Cartesian box and its implementation in code. We apply the code to a known analytic solution to verify that it works as expected. We perform the calculation at four different numerical resolutions to determine how this affects the convergence and numerical accuracy of the method as well as the calculation time.

We find that the fixed-point iteration converges in the sense that the change in the magnetic field between iterations, as measured by the metric ΔB_{\max} (Equation (51)), decreases by approximately six orders of magnitude over 20 iterations. The decrease in ΔB_{\max} appears to be exponential with a rate that does not depend strongly on the number of grid points. Although the method converged for all the cases presented, we found that if the resolution was made very low, by either using a small N or a large domain, then the method would not reach a fixed point. In this limit, we expect that the solution was dominated by the numerical truncation error.

We also measure the numerical truncation error of the method by comparing the known analytic solution to the numerical solution. We do this for calculations

at four different resolutions in order to establish a scaling law for the truncation error. We find that for the metric u_{\max} , which is sensitive to the maximum truncation error, the power-law index is -1.35 , as determined by a fit to the data. For the metric u_{avg} , which is sensitive to the average truncation error, we find the power-law index of the fit is -1.55 . The theoretical maximum truncation error in the field-line tracing solution to the hyperbolic equations is expected to have $\sim 1/N$ scaling (see the discussion in Gilchrist and Wheatland, 2013), while the maximum truncation error for the second-order finite-difference solution to the elliptic equations is expected to have $\sim 1/N^2$ scaling. These represent worst-case error estimates and in practice we would expect to find a power-law index for the truncation error somewhere in between one and two, which is what we find. We note some departure from the fit for u_{\max} at $N = 256$. The value here is approximately half that at $N = 128$, so while it does not lie on the fitted line, it is still consistent with the maximum theoretical error scaling of $\sim 1/N$.

We also perform a visual comparison between the field lines of the numerical and analytic solutions. After 20 iterations, the two sets are almost indistinguishable, except for field lines in the lower corners of panels (b) and (d) in Figure 3. We found that the field lines in this region can change significantly with even small changes in the electric current density. The region may have the largest error because the analytic solution in this region departs significantly from the initial potential field. The magnetic field in this region is also very weak compared with the field at the center of the domain. We emphasize that the discrepancy decreases with resolution (as can be seen in Figure 3), and would not appear to be due to the local failure of the method.

We also establish a scaling law for the total execution time of the code. We find that for a grid with N grid points in each dimension, the total run time has $\sim N^4$ scaling. This scaling is consistent with force-free codes based on the Grad-Rubin method (Wheatland, 2006). As in the case of the force-free codes, the time-consuming step is the field line tracing. We note that although the

scaling is similar, the magnetohydrostatic code is significantly slower in absolute terms because a single iteration of the magnetohydrostatic method involves more stages than the force-free Grad-Rubin method.

Our method requires that all field lines connect to the boundary, but no actual constraints on the connectivity are imposed during the iteration to enforce this. In one sense this is an advantage of the method, because it means the method can compute solutions whose topologies differ significantly from the magnetic field used to initiate the calculation. However, in another sense it is a weakness, because there is nothing to prevent closed field lines from forming during the calculation, at which point the calculation cannot proceed. We find that in our tests the appearance of closed field lines is generally in response to the formation of strong electric currents in weak-field regions. Future versions of the method could solve a more general formulation of the boundary-value problem that accounts for closed field lines. Despite this limitation, the method is still applicable to a range of interesting problems.

Finally, we note that the test case used is particularly simple. In particular, because it is untwisted, step iv) of the method is not tested. The numerical methods are similar to those used to solve step i), and we have tested the method on analytic solutions with a finite σ but no gravity, and we have found that the known solution is well reproduced. This gives us confidence that the method would work when applied to a case with both a finite twist and gravity force. We stress that although the test case was axisymmetric, since we work in Cartesian coordinates, our calculation was three-dimensional.

The work presented here has several limitations that could be addressed with future work. The fixed-point method could be generalized to explicitly model the energetics via an energy equation similar to the approach of Pizzo, MacGregor, and Kunasz (1993). Regarding the code itself, no significant optimization has yet been performed on the current first version, which could be addressed in the

future.

In this article we present a new iterative method for solving the magnetohydrostatic equations in a three-dimensional Cartesian domain and the details of an implementation of the method in code. We use our code to reconstruct a known analytic solution and thereby establish the correctness of the code and the viability of the method in general. This work is a step towards the generation of realistic three-dimensional magnetohydrostatic models of the solar atmosphere.

Appendix A

In this appendix we explain why the decomposition of the pressure into a magnetohydrostatic and a hydrostatic components presented in Section 2.2 is necessary for the stability of the fixed-point method. We find that without solving for these components separately, an instability occurs due to the failure to achieve exact hydrostatic force balance in weak-field regions.

In terms of the total pressure, p , and density, ρ , the update equation for the perpendicular electric current density is

$$\mathbf{J}_{\perp}^{[k+1]} = \frac{-\nabla p^{[k+1]} \times \mathbf{B}^{[k]} + \rho^{[k+1]} \mathbf{g} \times \mathbf{B}^{[k]}}{\|\mathbf{B}^{[k]}\|^2}. \quad (55)$$

Using this equation rather than Equation (26) results in the formation of spurious electric currents in weak-field regions, where the denominator becomes small but the numerator remains finite due to numerical error. To understand this, let p and ρ be split as in Section 2.2. Equation (55) then becomes

$$\mathbf{J}_{\perp}^{[k+1]} = \frac{(-\nabla p_{\text{mhs}}^{[k+1]} \times \mathbf{B}^{[k]} + \rho_{\text{mhs}}^{[k+1]} \mathbf{g} \times \mathbf{B}^{[k]}) + (-\nabla p_{\text{hs}}^{[k+1]} \times \mathbf{B}^{[k]} + \rho_{\text{hs}}^{[k+1]} \mathbf{g} \times \mathbf{B}^{[k]})}{\|\mathbf{B}^{[k]}\|^2}. \quad (56)$$

In principle, the second term in the numerator is zero, however, in practice this is not achieved numerically, which introduces an error, $\epsilon(\mathbf{r})$, in the numerator. The

functional form of $\epsilon(\mathbf{r})$ depends on the details of the numerical implementation, but, in general, its magnitude varies with position and decreases with resolution. In weak-field regions p_{mhs} and ρ_{mhs} are small, and thus the perpendicular current density has scaling $\sim \epsilon/||\mathbf{B}^{[k]}||$. The hydrostatic component of the atmosphere is independent of the magnetic field, and so the error ϵ is not necessarily small in weak-field regions. This results in the formation of strong spurious currents in weak-field regions because the denominator $||\mathbf{B}^{[k]}||$ becomes small while the numerator remains finite. These currents can prevent the method from converging.

Appendix B

Here we provide the details of the pressure update step.

To update the pressure at each iteration it is necessary to solve the equations

$$\frac{dp_{\text{mhs}}}{ds} + F(s)p_{\text{mhs}} = G(s), \quad (57)$$

and

$$\frac{d\mathbf{x}}{ds} = -\frac{\mathbf{B}}{||\mathbf{B}||}, \quad (58)$$

in the volume at each Cartesian mesh point (x_i, y_j, z_k) . The functions $F(s)$ and $G(s)$ are defined by Equations (45) and (44), respectively. The boundary conditions are

$$\mathbf{x}|_{s=0} = (x_i, y_j, z_k), \quad (59)$$

and

$$p_{\text{mhs}}|_{s=s_0} = p_0, \quad (60)$$

where $x(s_0), y(s_0), z(s_0)$ is the point where the field line crosses the boundary with the polarity over which boundary conditions are prescribed.

This is not an initial-value problem because \boldsymbol{x} and p are not known simultaneously at either s or s_0 . Application of a standard iterative method for solving ordinary-differential equations (like the Runge-Kutta method) is therefore impossible, because the iteration cannot be initialized without knowledge of both \boldsymbol{x} and p at the same point. The problem, however, can be reformulated into two auxiliary initial-value problems that can be solved with a straightforward application of standard methods.

First consider p_a , which is the solution to the equation

$$\frac{dp_a}{ds} + F(s)p_a = G(s), \quad (61)$$

with initial condition $p_a(0) = A$. Also consider p_b , which is the solution of the homogeneous equation

$$\frac{dp_b}{ds} + F(s)p_b = 0, \quad (62)$$

with $p_b(0) = B$. In both cases the equation and initial condition for \boldsymbol{x} are the same as the original problem. Note that λp_b , where λ is a scalar, is also a solution to Equation (62). It follows that, since Equation (57) is linear,

$$p_c = p_a + \lambda p_b, \quad (63)$$

is also solution of Equation (57). The variable λ can be treated as a free parameter and chosen such that $p_c = p_0$ at the point where the field line crosses the boundary, *i.e.*

$$\lambda = (p_0 - p_a(s_0))/p_b(s_0). \quad (64)$$

With this choice, p_c is a solution to the original boundary-value problem: it satisfies Equation (57) and the boundary conditions defined by Equation (60).

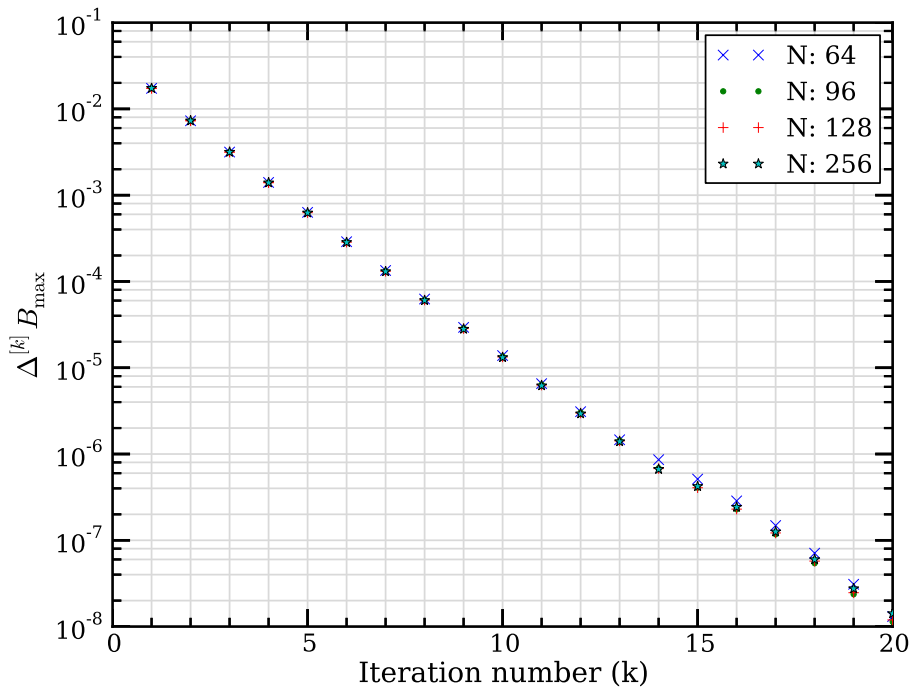


Figure 1. Change in the magnetic field between successive iterations as measured by the ΔB_{\max} metric for the four test cases. Each calculation is performed with a different grid size N .

It follows that the value of p_{mhs} at the point $s = 0$, with Cartesian coordinates (x_i, y_j, z_k) , is

$$p_{\text{mhs}}(0) = p_a(0) + \lambda p_b(0) = A + B\lambda. \quad (65)$$

Hence the solution to the boundary-value problem can be found by computing λ , which requires solving the two initial-value problems for p_a and p_b . The simplest choice for the constants A and B is $A = 0$ and $B = 1$, although other combinations are possible. The initial-value problems for p_a and p_b are in the standard form and can be treated using a straightforward application of a method like Runge-Kutta.

Acknowledgments Support for this work is provided by the NASA Living With a Star program through grant NNX14AD42G, and by the Solar Terrestrial program of the National Science Foundation through grant AGS-1127327.

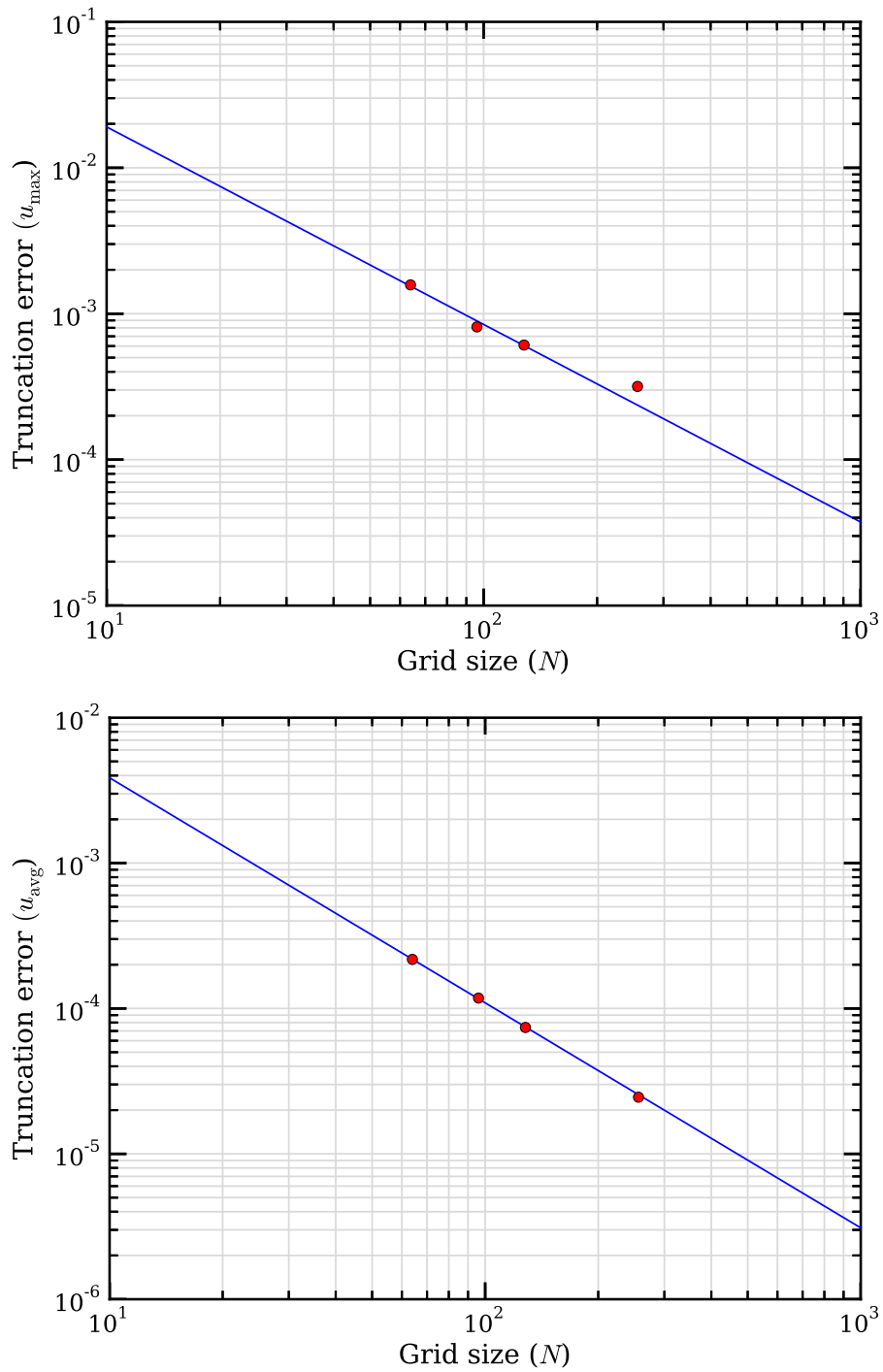


Figure 2. Truncation error *versus* grid resolution as measured by the u_{\max} (top panel) and u_{avg} (bottom panel) metrics. The solid lines are power-law fits to the data with power-law indices -1.35 (top panel) and -1.55 (bottom panel).

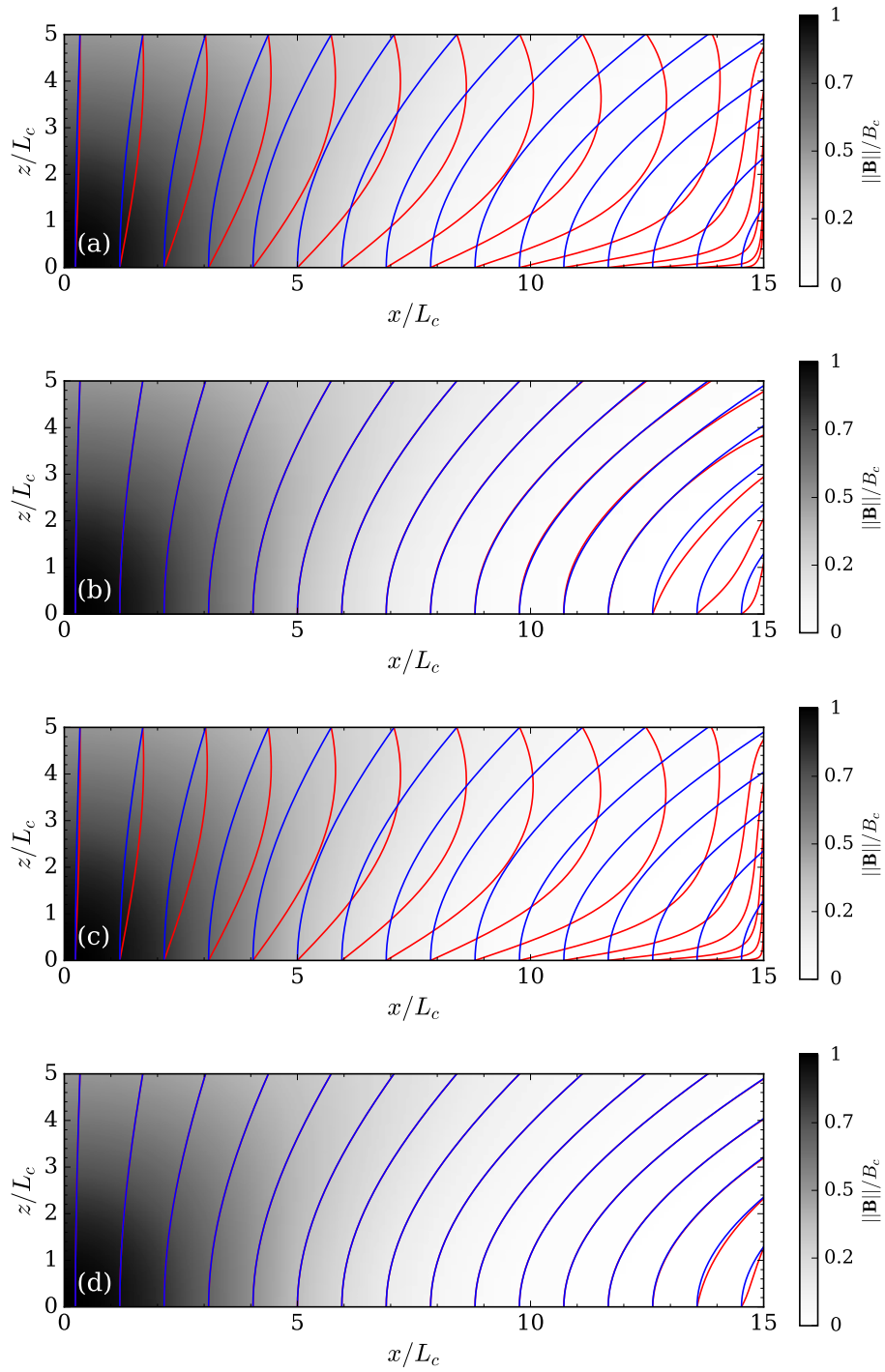


Figure 3. Field lines of the exact solution (blue) superimposed on those of the numerical solutions (red) in the $x - z$ plane through the origin. In panels (a) and (b), the red field lines belong to the initial potential field and the solution after 20 iterations of the fixed-point method, respectively, for the calculation with $N = 64$. Panels (c) and (d) show the same for the $N = 256$ calculation. In all panels the field lines are traced from starting points spaced equally along the x axis, meaning the density of field lines is not indicative of field strength.

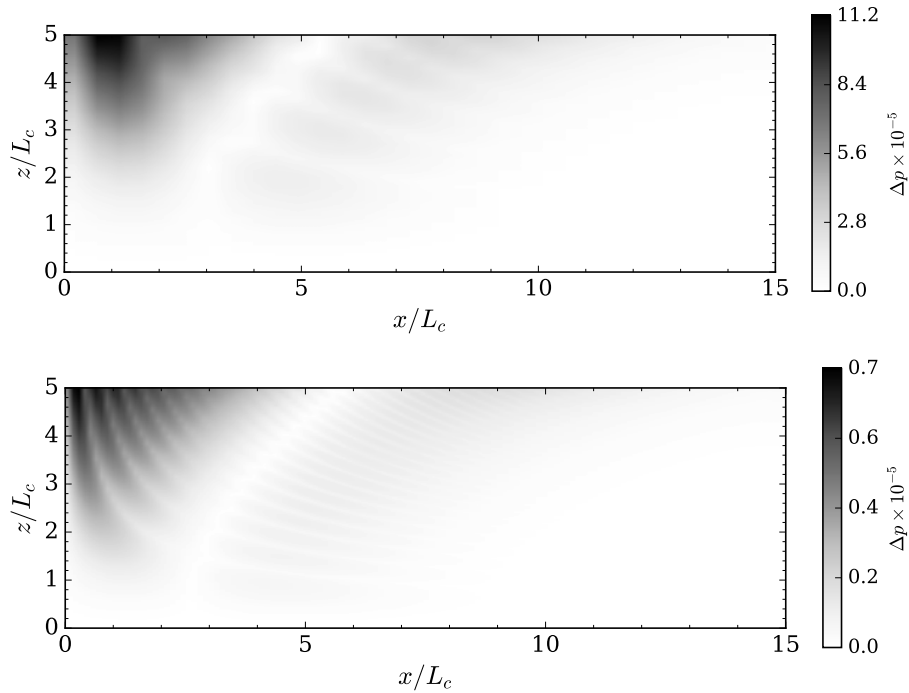


Figure 4. The normalized absolute difference (see Equation 54) between the pressure of the analytic solution and the numerical solution after 20 iterations of the method for $N = 64$ (top panel) and $N = 256$ (bottom panel). Note that the scales on the color bars are different.

Disclosure of Potential Conflicts of Interest The authors declare that they have no conflicts of interest.

References

- Amari, T., Boulbe, C., Boulmezaoud, T.Z.: 2009, Computing beltrami fields. *SIAM J. Scien. Compt.* **31**(5), 3217. DOI.
- Amari, T., Boulmezaoud, T.Z., Mikic, Z.: 1999, An iterative method for the reconstruction-break of the solar coronal magnetic field. I. Method for regular solutions. *Astron. Astrophys.* **350**, 1051. ADS.
- Amari, T., Aly, J.-J., Canou, A., Mikic, Z.: 2013, Reconstruction of the solar coronal magnetic field in spherical geometry. *Astron. Astrophys.* **553**, A43. DOI. ADS.
- Aulanier, G., Démoulin, P., Schmieder, B., Fang, C., Tang, Y.H.: 1998, Magnetohydrostatic Model of a Bald-Patch Flare. *Solar Phys.* **183**, 369. DOI. ADS.
- Aulanier, G., Démoulin, P., Mein, N., van Driel-Gesztelyi, L., Mein, P., Schmieder, B.: 1999, 3-D magnetic configurations supporting prominences. III. Evolution of fine structures observed in a filament channel. *Astron. Astrophys.* **342**, 867. ADS.

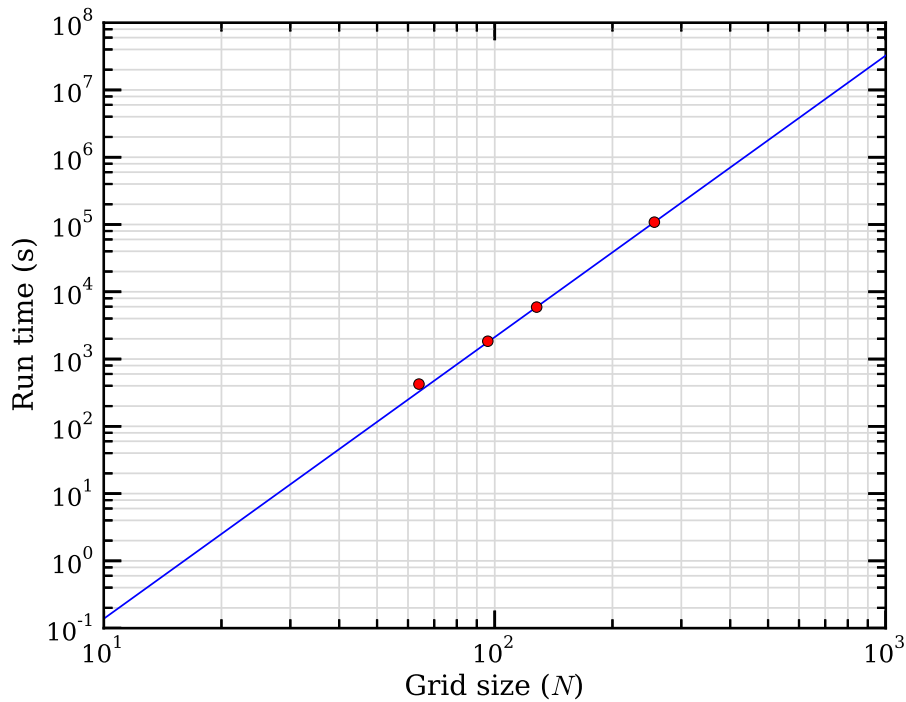


Figure 5. Total time to complete 20 iterations of the fixed-point method *versus* grid size N . The straight line is a power-law fit to the data with power-law index of 4.2.

Bogdan, T.J., Low, B.C.: 1986, The three-dimensional structure of magnetostatic atmospheres.

II - Modeling the large-scale corona. *Astrophys. J.* **306**, 271. DOI. ADS.

Briggs, W.L., Henson, V.E., McCormick, S.F.: 2000, *A multigrid tutorial (2nd ed.)*, Society for Industrial and Applied Mathematics, Philadelphia, PA, USA. ISBN 0-89871-462-1. DOI.

Cally, P.S.: 1990, An inverse coordinate multigrid method for free boundary magnetohydrostatics. *J. Comput. Phys.* **89**, 490. DOI. ADS.

Cameron, R.H., Gizon, L., Schunker, H., Pietarila, A.: 2011, Constructing Semi-Empirical Sunspot Models for Helioseismology. *Solar Phys.* **268**, 293. DOI. ADS.

Chandra, R., Dagum, L., Kohr, D., Maydan, D., McDonald, J., Menon, R.: 2001, *Parallel programming in openmp*, Morgan Kaufmann Publishers Inc., San Francisco, CA, USA. ISBN 1-55860-671-8, 9781558606715.

Chodura, R., Schlüter, A.: 1981, A 3d code for mhd equilibrium and stability. *Journal of Computational Physics* **41**(1), 68 . DOI.

Deinzer, W., Hensler, G., Schuessler, M., Weisshaar, E.: 1984, Model calculations of magnetic flux tubes. I - Equations and method. II - Stationary results for solar magnetic elements. *Astron. Astrophys.* **139**, 426. ADS.

DeRosa, M.L., Schrijver, C.J., Barnes, G., Leka, K.D., Lites, B.W., Aschwanden, M.J., Amari, T., Canou, A., McTiernan, J.M., Régnier, S., Thalmann, J.K., Valori, G., Wheatland, M.S.,

-
- Wiegelmann, T., Cheung, M.C.M., Conlon, P.A., Fuhrmann, M., Inhester, B., Tadesse, T.: 2009, A Critical Assessment of Nonlinear Force-Free Field Modeling of the Solar Corona for Active Region 10953. *Astrophys. J.* **696**, 1780. DOI. ADS.
- DeRosa, M.L., Wheatland, M.S., Leka, K.D., Barnes, G., Amari, T., Canou, A., Gilchrist, S.A., Thalmann, J.K., Valori, G., Wiegelmann, T., Schrijver, C.J., Malanushenko, A., Sun, X., Régnier, S.: 2015, The Influence of Spatial resolution on Nonlinear Force-free Modeling. *Astrophys. J.* **811**, 107. DOI. ADS.
- Fiedler, R.A.S., Cally, P.S.: 1990, Force and energy balance in the transition region network. *Solar Phys.* **126**, 69. DOI. ADS.
- Gary, G.A.: 2001, Plasma Beta above a Solar Active Region: Rethinking the Paradigm. *Solar Phys.* **203**, 71. DOI. ADS.
- Gilchrist, S.A., Wheatland, M.S.: 2013, A Magnetostatic Grad-Rubin Code for Coronal Magnetic Field Extrapolations. *Solar Phys.* **282**, 283. DOI. ADS.
- Gilchrist, S.A., Wheatland, M.S.: 2014, Nonlinear Force-Free Modeling of the Corona in Spherical Coordinates. *Solar Phys.* **289**, 1153. DOI. ADS.
- Gilchrist, S.A., Wheatland, M.S., Leka, K.D.: 2012, The Free Energy of NOAA Solar Active Region AR 11029. *Solar Phys.* **276**, 133. DOI. ADS.
- Grad, H., Rubin, H.: 1958, Hydromagnetic equilibria and force-free fields. In: Martens, J.H., Oourom, L., Barss, W.M., Bassett, L.G., Smith, K.R.E., Gerrard, M., Hudswell, F., Guttman, B., Pomeroy, J.H., Woollen, W.B., Singwi, K.S., Carr, T.E.F., Kolb, A.C., Matterson, A.H.S., Welgos, S.P., Rojanski, I.D., Finkelstein, D. (eds.) *Peaceful Uses of Atomic Energy: Theoretical and Experimental Aspects of Controlled Nuclear Fusion* **31**, United Nations, Geneva, 190.
- Greene, J.M., Johnson, J.L.: 1961, Determination of hydromagnetic equilibria. *Physics of Fluids* **4**(7), 875. DOI.
- Hairer, E., Nørsett, S.P., Wanner, G.: 1993, *Solving ordinary differential equations i (2nd revised. ed.): Nonstiff problems*, Springer, New York, NY, USA, 195. ISBN 0-387-56670-8. DOI.
- Hennig, B.S., Cally, P.S.: 2001, Numerical Solutions of Three-Dimensional Pressure-Bounded Magnetohydrostatic Flux Tubes. *Solar Phys.* **201**, 289. DOI. ADS.
- Khomenko, E., Collados, M.: 2006, Numerical Modeling of Magnetohydrodynamic Wave Propagation and Refraction in Sunspots. *Astrophys. J.* **653**, 739. DOI. ADS.
- Khomenko, E., Collados, M., Felipe, T.: 2008, Nonlinear Numerical Simulations of Magneto-Acoustic Wave Propagation in Small-Scale Flux Tubes. *Solar Phys.* **251**, 589. DOI. ADS.
- Kippenhahn, R., Schlüter, A.: 1957, Eine Theorie der solaren Filamente. Mit 7 Textabbildungen. *Zeitschrift Astrophysik* **43**, 36. ADS.
- Low, B.C.: 1980, Exact static equilibrium of vertically oriented magnetic flux tubes. I - The Schlueter-Temesvary sunspot. *Solar Phys.* **67**, 57. DOI. ADS.
- Low, B.C.: 1984, Three-dimensional magnetostatic atmospheres - Magnetic field with vertically oriented tension force. *Astrophys. J.* **277**, 415. DOI. ADS.

-
- Low, B.C.: 1985, Three-dimensional structures of magnetostatic atmospheres. I - Theory. *Astrophys. J.* **293**, 31. DOI. ADS.
- Low, B.C.: 1992, Three-dimensional structures of magnetostatic atmospheres. IV - Magnetic structures over a solar active region. *Astrophys. J.* **399**, 300. DOI. ADS.
- Metcalf, M., Reid, J., Cohen, M.: 2011, *Modern fortran explained*, 4th edn. Oxford University Press, Inc., New York, NY, USA. ISBN 0199601410, 9780199601417.
- Metcalf, T.R., Jiao, L., McClymont, A.N., Canfield, R.C., Uitenbroek, H.: 1995, Is the solar chromospheric magnetic field force-free? *Astrophys. J.* **439**, 474. DOI. ADS.
- Moradi, H., Hanasoge, S.M., Cally, P.S.: 2009, Numerical Models of Travel-Time Inhomogeneities in Sunspots. *Astrophys. J. Lett.* **690**, L72. DOI. ADS.
- Moradi, H., Baldner, C., Birch, A.C., Braun, D.C., Cameron, R.H., Duvall, T.L., Gizon, L., Haber, D., Hanasoge, S.M., Hindman, B.W., Jackiewicz, J., Khomenko, E., Komm, R., Rajaguru, P., Rempel, M., Roth, M., Schlichenmaier, R., Schunker, H., Spruit, H.C., Strassmeier, K.G., Thompson, M.J., Zharkov, S.: 2010, Modeling the Subsurface Structure of Sunspots. *Solar Phys.* **267**, 1. DOI. ADS.
- Neukirch, T.: 1997, Nonlinear self-consistent three-dimensional arcade-like solutions of the magnetohydrostatic equations. *Astron. Astrophys.* **325**, 847. ADS.
- Petrie, G.J.D.: 2000, Three-dimensional Equilibrium Solutions to the Magnetohydrodynamic Equations and their Application to Solar Coronal Structures. PhD thesis, Univ. of St. Andrews. ADS.
- Petrie, G.J.D., Neukirch, T.: 2000, The Green's function method for a special class of linear three-dimensional magnetohydrostatic equilibria. *Astron. Astrophys.* **356**, 735. ADS.
- Pizzo, V.J.: 1986, Numerical solution of the magnetostatic equations for thick flux tubes, with application to sunspots, pores, and related structures. *Astrophys. J.* **302**, 785. DOI. ADS.
- Pizzo, V.J.: 1990, Numerical modeling of solar magnetostatic structures bounded by current sheets. *Astrophys. J.* **365**, 764. DOI. ADS.
- Pizzo, V.J., MacGregor, K.B., Kunasz, P.B.: 1993, A numerical simulation of two-dimensional radiative equilibrium in magnetostatic flux tubes. I - The model. *Astrophys. J.* **404**, 788. DOI. ADS.
- Pneuman, G.W., Kopp, R.A.: 1971, Gas-Magnetic Field Interactions in the Solar Corona. *Solar Phys.* **18**, 258. DOI. ADS.
- Press, W.H., Teukolsky, S.A., Vetterling, W.T., Flannery, B.P.: 2007, *Numerical recipes 3rd edition: The art of scientific computing*, 3rd edn. Cambridge University Press, New York, NY, USA, 150. ISBN 0521880688, 9780521880688.
- Priest, E.: 2014, *Magnetohydrodynamics of the sun*, Cambridge University Press, Cambridge, UK, 133. ISBN 9781139020732. DOI. ADS.
- Régnier, S., Amari, T., Kersalé, E.: 2002, 3D Coronal magnetic field from vector magnetograms: non-constant-alpha force-free configuration of the active region NOAA 8151. *Astron. Astrophys.* **392**, 1119. DOI. ADS.
- Ruan, P., Wiegmann, T., Inhester, B., Neukirch, T., Solanki, S.K., Feng, L.: 2008, A first

-
- step in reconstructing the solar corona self-consistently with a magnetohydrostatic model during solar activity minimum. *Astron. Astrophys.* **481**, 827. DOI. ADS.
- Sakurai, T.: 1981, Calculation of force-free magnetic field with non-constant α . *Solar Phys.* **69**, 343. DOI. ADS.
- Schlüter, A., Temesváry, S.: 1958, The Internal Constitution of Sunspots. In: Lehnert, B. (ed.) *Electromagnetic Phenomena in Cosmical Physics, IAU Symp.* **6**, 263. ADS.
- Socas-Navarro, H.: 2005, The Three-dimensional Structure of a Sunspot Magnetic Field. *Astrophys. J. Lett.* **631**, L167. DOI. ADS.
- Spitzer, L. Jr.: 1958, The Stellarator Concept. *Physics of Fluids* **1**, 253. DOI. ADS.
- Steiner, O., Pneuman, G.W., Stenflo, J.O.: 1986, Numerical models for solar magnetic fluxtubes. *Astron. Astrophys.* **170**, 126. ADS.
- Thalmann, J.K., Wiegmann, T., Raouafi, N.-E.: 2008, First nonlinear force-free field extrapolations of SOLIS/VSM data. *Astron. Astrophys.* **488**, L71. DOI. ADS.
- Uchida, Y., Low, B.C.: 1981, Equilibrium configuration of the magnetosphere of a star loaded with accreted magnetized mass. *J. Astrophys. Astron.* **2**, 405. DOI. ADS.
- Valori, G., Green, L.M., Démoulin, P., Vargas Domínguez, S., van Driel-Gesztelyi, L., Wallace, A., Baker, D., Fuhrmann, M.: 2012, Nonlinear Force-Free Extrapolation of Emerging Flux with a Global Twist and Serpentine Fine Structures. *Solar Phys.* **278**, 73. DOI. ADS.
- Vernazza, J.E., Avrett, E.H., Loeser, R.: 1981, Structure of the solar chromosphere. III - Models of the EUV brightness components of the quiet-sun. *Astron. Astrophys. Suppl.* **45**, 635. DOI. ADS.
- Wheatland, M.S.: 2004, Parallel Construction of Nonlinear Force-Free Fields. *Solar Phys.* **222**, 247. DOI. ADS.
- Wheatland, M.S.: 2006, A Fast Current-Field Iteration Method for Calculating Nonlinear Force-Free Fields. *Solar Phys.* **238**, 29. DOI. ADS.
- Wheatland, M.S.: 2007, Calculating and Testing Nonlinear Force-Free Fields. *Solar Phys.* **245**, 251. DOI. ADS.
- Wheatland, M.S., Régnier, S.: 2009, A Self-Consistent Nonlinear Force-Free Solution for a Solar Active Region Magnetic Field. *Astrophys. J. Lett.* **700**, L88. DOI. ADS.
- Wheatland, M.S., Sturrock, P.A., Roumeliotis, G.: 2000, An Optimization Approach to Reconstructing Force-free Fields. *Astrophys. J.* **540**, 1150. DOI. ADS.
- Wiegmann, T., Inhester, B.: 2003, Magnetic modeling and tomography: First steps towards a consistent reconstruction of the solar corona. *Solar Phys.* **214**, 287. DOI. ADS.
- Wiegmann, T., Neukirch, T., Ruan, P., Inhester, B.: 2007, Optimization approach for the computation of magnetohydrostatic coronal equilibria in spherical geometry. *Astron. Astrophys.* **475**, 701. DOI. ADS.
- Wiegmann, T., Neukirch, T., Nickeler, D.H., Solanki, S.K., Martínez Pillet, V., Borrero, J.M.: 2015, Magneto-static Modeling of the Mixed Plasma Beta Solar Atmosphere Based on Sunrise/IMaX Data. *Astrophys. J.* **815**, 10. DOI. ADS.
- Zweibel, E.G., Hundhausen, A.J.: 1982, Magnetostatic atmospheres - A family of isothermal

solutions. *Solar Physics* **76**, 261. DOI. ADS.